

Electrochemical and AFM study of nickel nucleation mechanisms on vitreous carbon from ammonium sulfate solutions

Darko Grujicic, Batric Pesic*

University of Idaho, College of Engineering, Department of Materials Science and Engineering, McClure Hall, Moscow, ID 83844-3024, USA

Received 22 February 2005; received in revised form 7 May 2005; accepted 7 August 2005

Available online 19 September 2005

Abstract

Reaction and nucleation mechanisms of nickel in ammoniacal solutions have been investigated as a function of nickel concentration, solution pH, deposition potential, temperature and conditioning potential. Electrochemical mechanisms of nickel reduction were found to be pH dependent, while their kinetics was concentration dependent. A surface film formed by anodic oxidation passivates nickel clusters preventing their further oxidation. Nickel nucleation on vitreous carbon, which proceeds according to the progressive nucleation model, shows a large degree of inhibition at both pH 6 and pH 9. Cluster sizes were larger when electrodeposition was carried out from solutions with higher nickel concentrations. The clusters were also larger at more negative deposition potentials and at higher solution pH. Cluster population density increased with the increasing solution temperature. Different activation energies for the nickel–aquo and nickel–amino complexes calculated from Arrhenius diagram indicate that electroreduction of nickel–amino complex is energetically more demanding. All electrochemical results were further verified by the atomic force microscopy investigations.

© 2005 Elsevier Ltd. All rights reserved.

Keywords: Nickel electrodeposition; Ammonia; Nucleation; Electrode conditioning; Atomic force microscopy—AFM

1. Introduction

Nickel coatings are among the earliest commercially electrodeposited thin metallic films [1,2]. The first nickel bath was formulated by Watts [3] in 1916, and this bath is still used today because of its simplicity to control and low cost to operate. Although the literature body on nickel electrodeposition is voluminous, the attention will be paid mostly to the area of nickel nucleation mechanisms. This area of research is predominantly driven by the application of nickel electrochemistry for fuel cell development, resulting in numerous nickel nucleation studies, mostly on vitreous carbon as the preferred substrate [4–11].

The mechanisms of nickel deposition, derived from the chronoamperometric current transients [4–9], indicate that nickel nucleation on vitreous carbon proceeds through formation of discrete nuclei, of conical [4–6] or hemispherical

shape [7], of non-uniform size (i.e. progressive nucleation) [9,11]. Progressive nickel nucleation can be inhibited by adsorption of nickel hydroxide [12], and by formation of nickel hydrides due to concurrent reduction of hydrogen ions [10]. Typical surface coverage by nickel ad-atoms required to initiate nickel nucleation on vitreous carbon found [8] was in the range 1–5%.

From the reaction point of view, the most frequently cited mechanisms [13,14] for nickel electrodeposition from acidic chloride solutions containing high nickel concentration involve two consecutive one-electron charge-transfer steps, with adsorption of intermediary cationic Ni complex, reactions (1)–(3):



However, the reaction mechanisms for acidic electrolytes of the Watts type is not universally accepted [15]. The reac-

* Corresponding author. Tel.: +1 208 885 6569; fax: +1 208 885 2855.
E-mail address: pesic@uidaho.edu (B. Pesic).

tion mechanisms for basic solutions, involving another complexing agent, ammonia, are not consistent either. Thus, the study by Davison and Harrison [16] implies that reduction of nickel–ammonia complexes proceeds through a single, two-electron charge-transfer step, which is in contrast to the study by Philip and Nicol [17], who found that nickel electrodeposition is a two-stage single-electron process.

Because most of the nickel nucleation studies were performed in acidic solutions of Watts type, leaving the ammoniacal systems relatively unexplored, or incomplete [18], it was decided to launch a comprehensive nickel nucleation study in the later, ammoniacal, solutions. The experimental techniques used were cyclic voltammetry and chronoamperometry in combination with the morphological characterization by atomic force microscopy. Vitreous carbon was selected as electrode material.

2. Experimental

Reagent grade $\text{NiSO}_4 \cdot 5\text{H}_2\text{O}$ was used to prepare 0.005 M, 0.01 M and 0.05 M Ni^{2+} solutions. Solutions were prepared with deionized water (Type I purity water, Barnstead NANOpure II, 18.2 M Ω). All solutions contained 1 M reagent grade $(\text{NH}_4)_2\text{SO}_4$ that served both as a buffer and as a supporting electrolyte. The solutions were adjusted to pH 6 or pH 9 by addition of dilute H_2SO_4 or NH_4OH , respectively. Deaeration of the solution in the electrochemical cell (15 ml) by argon gas purging for 10 min, with the electrode retracted from the solution, preceded each electrochemical experiment. All experiments were run under quiescent conditions, and only freshly prepared solutions were used.

The electrochemical setup was a standard three-electrode cell, with vitreous carbon as a working electrode, platinum foil as a counter electrode, and a silver–silver chloride reference electrode (Cypress Systems microelectrode, $E_h^0 = +0.222\text{V}$). The vitreous carbon working electrode (0.442 cm 2) was a non-porous disk (Sigri). The working electrode was prepared by polishing with successively finer grades of abrasive paper, followed by wet polishing with 1 μm and 0.05 μm alumina on a wet polishing cloth. The final step was polishing with dry 0.05 μm alumina on a coarsely sanded glass plate. The electrode was then sonicated briefly in deionized water to remove remaining alumina particles, and then dried in a stream of nitrogen gas. This method of surface preparation provides both electrochemically reproducible surface properties (tested by measuring the peak separation of ferrous/ferric cyanide redox couple), and roughness (root mean square) close to 1 nm that is suitable for the nucleation studies. Only the dry polishing step was repeated after every electrochemical experiment, which was found to be sufficient to electrochemically re-activate the surface, while reducing the polishing time required to achieve low surface roughness. Electrochemical experiments were executed by a potentiostat/galvanostat (Ametek, PAR 273A) controlled by a PC running the electrochemical software (PAR, M270).

Upon the completion of the experiment, surface morphology of nickel deposits was characterized *ex situ* by atomic force microscopy (VEECO, Digital Instruments, Model Nanoscope IIIa-MultiMode, tapping mode in fluid). Nickel deposits were characterized *ex situ*, under the protective layer of cyclohexane in order to prevent oxidation by oxygen from air. Distribution–pH diagrams were constructed by using thermochemical software Stabcal [19].

3. Results and discussion

3.1. Nickel ammonia chemistry

Nickel ion in aqueous solutions has octahedral coordination, similar to those of copper and cobalt, which allows for accommodation of six ligands in its first hydration shell. For each of the solution compositions in this study, the speciation of nickel in ammonia solution was examined by constructing the distribution–pH diagrams. Two such diagrams are presented in Fig. 1a and b.

There are four characteristic pH regions in Fig. 1a and b. The first region is characterized by the free nickel ion as the most stable species (pH region 0–1.5). In the second region, between pH 1.5 and pH 8, the predominant nickel species is a soluble, negatively charged sulfate complex.

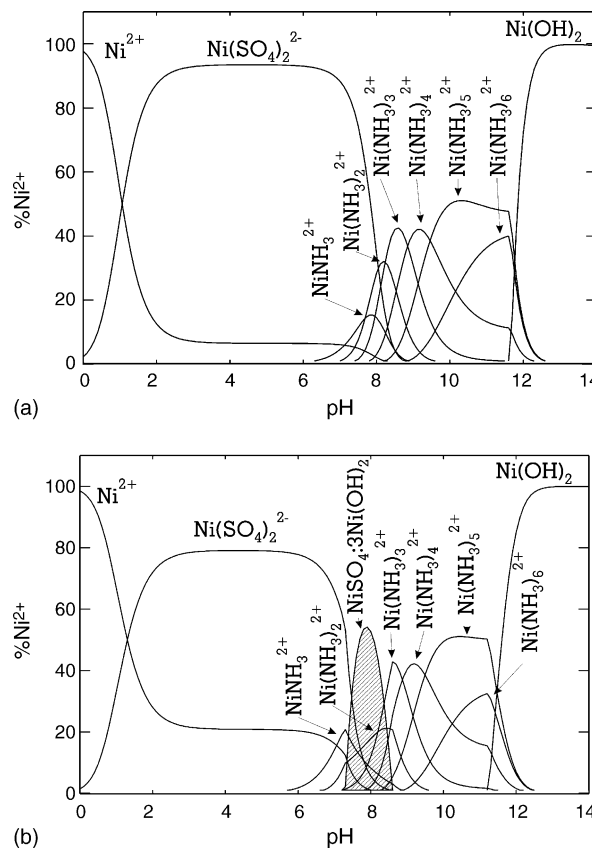


Fig. 1. Distribution–pH diagram for: (a) 0.01 M Ni^{2+} and (b) 0.05 M Ni^{2+} in 1 M $(\text{NH}_4)_2\text{SO}_4$ solution. Note the appearance of hydroxy–sulfate (shaded) in (b).

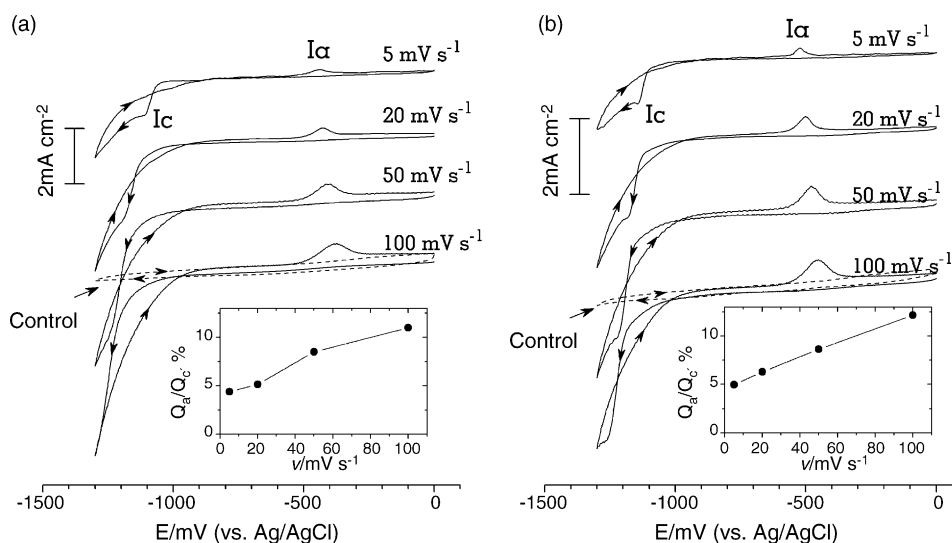


Fig. 2. Effect of scanning rate on the cyclic voltammograms for nickel–ammonia system at: (a) pH 6 and (b) pH 9. For comparison, dashed lines in (a) and (b) are control cv-s containing no nickel ions. Insets represent the ratio of anodic to cathodic charge as a function of the scanning rate. Conditions: 0.005 M Ni²⁺; 1 M (NH₄)₂SO₄.

In the third region, from pH 8 to pH 12, there is a series of nickel–ammonia complexes with successively increasing number of incorporated ammonia ligands, NiNH₃²⁺ to Ni(NH₃)₆²⁺. In 0.05 M Ni²⁺ solution, nickel hydroxy–sulfate precipitates in the third region around pH 8. The fourth region, beyond pH 12, is characterized by nickel hydroxide as the only thermodynamically stable species. Representative solutions for the present study were taken from the second and third region, i.e. pH 6 was representing a nickel–sulfate complex, while pH 9 was representing nickel–ammonia complexes. The instability of 0.05 M Ni²⁺ solutions due to precipitation of nickel hydroxy–sulfate has limited the investigations for this nickel concentration only to cyclic voltammetry.

3.2. Cyclic voltammetry

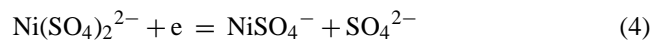
Cyclic voltammograms for the investigated solutions were run from the initial voltage of 0 mV to the vertex potential of –1300 mV, and returned to the initial voltage. A typical set of cyclic voltammograms is presented in Fig. 2a and b.

According to Fig. 2a and b, the cyclic voltammograms for each pH are characterized by one cathodic and one anodic peak. The cv-s also include a loop characteristic for electrodeposition [20].

Based on the thermodynamic speciation in Fig. 1a and b and the results of cyclic voltammetry (Fig. 2a and b), the reaction mechanisms for nickel electrodeposition are categorized according to the solution pH as described below.

At pH 6, nickel electrodeposition proceeds in three, two electrochemical and one adsorption, steps. In the first electroreduction step (reaction (4)), nickelous sulfate ions is formed, followed by its surface adsorption (reaction (5)). The second electroreduction step is responsible for deposition of

metallic nickel (reaction (6)).



According to Davison and Harrison [16], for 0.005 M Ni²⁺ concentration the chemical step of adsorption of nickel–sulfate complex on glassy carbon is fast, i.e. both electrochemical reactions are seen, as the overall rate-controlling step is the reaction (6). With the increasing nickel ions concentration, the chemical step of NiSO₄⁻ adsorption, reaction (5), becomes the rate-controlling step, as confirmed by the studies of nickel electrodeposition from more concentrated solutions [13–15,17].

The variation in the rate of NiSO₄⁻ adsorption is most likely related to the available type of deposition substrate. Below certain Ni concentration range, the predominant deposition substrate is glassy carbon, and vice versa, deposited nickel metal becomes the deposition substrate for higher concentration range. It is known that the concentration of nickel ad-atoms on glassy carbon increases with the increase of nickel ions concentration [8]. Low nickel concentrations result in low glassy carbon surface coverage by nickel ad-atoms, and consequently sparse nuclei population, i.e. glassy carbon surface will mostly stay free. Because the adsorption rate of NiSO₄⁻ on metallic nickel is slow, due to inhibition by adsorbed species (H_(ads) and SO_{4(ads)}²⁻) [9,12–14,21], the adsorption and discharge of NiSO₄⁻ on glassy carbon becomes the preferred route. As the result, glassy carbon surface becomes covered by a large number of very small nickel clusters in the initial stages of nickel electrodeposition. For high nickel concentrations, the glassy carbon surface cover-

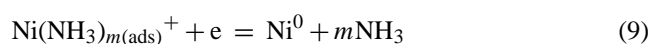
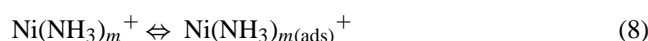
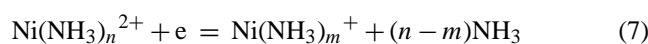
age with nickel clusters is extensive, almost complete, thus NiSO_4^- adsorption and subsequent reduction has to happen on nickel surface. However, as already stated, because the adsorption rate of NiSO_4^- on metallic nickel is slow, it becomes the rate-determining step.

The importance of adsorption during nickel deposition was recognized by Chassaing et al. [13], who discussed the inhibitory effects of H^+ and SO_4^{2-} ions. The inhibition by H^+ was the result of its reduction to atomic state, subsequent adsorption of H_{ads} atoms and nickel hydride formation. In this study, peak Ic was immediately followed by the increase of cathodic current that corresponds to reduction of hydrogen ions and formation of adsorbed hydrogen atoms, which recombined to form hydrogen gas. The question regarding the site for hydrogen ion reduction, glassy carbon versus nickel, was resolved by running control cv-s in nickel-free solutions (Fig. 2a and b). Zero current found demonstrates that the reduction on glassy carbon can be ruled out, i.e. that hydrogen ion reduction takes place only on the surface of newly formed nickel clusters, supporting the suggested inhibiting role of adsorbed hydrogen.

The inhibitory presence of SO_4^{2-} is the result of competitive occupation of adsorption sites on nickel surface. The electrode potential is essential for adsorption/desorption of SO_4^{2-} . During electrodeposition by scanning in cathodic direction, SO_4^{2-} ions undergo desorption process as the potential becomes more negative, as verified by the in situ scanning tunneling microscopy during electrodeposition of copper (Broekmann et al. [22], Wilms et al. [23] and Yan et al. [24]). In our recent study on copper electrodeposition, we were also able to confirm, by means of cyclic voltammetry, the sulfate desorption process. Similar approach was also used in this study. First, nickel was electrodeposited from nickel–ammonia solution at pH 6 at -1300 mV for 20 s. After deposition, the nickel–ammonia solution was replaced with 1 M Na_2SO_4 solution at either pH 3 or pH 6, and the cyclic voltammograms recorded in the region -700 mV to -1000 mV, where sulfate desorption was expected to take place. The results are presented in Fig. 3.

The peak observed for pH 3 solution in Fig. 3 corresponds to desorption of sulfate anions, and to a consequent adsorbate-induced hydrogen reduction reaction [22–24]. Because of the lower hydrogen ion concentration, the same peak at pH 6 is convoluted with the background current becoming more difficult to distinguish.

At pH 9, electrodeposition of nickel proceeds according to the mechanisms proposed by Davison and Harrison [16] and Philip and Nicol [17] (reactions (7)–(9)):



Reaction (9) represents the rate-controlling step at lower nickel concentrations [16], while at higher nickel con-

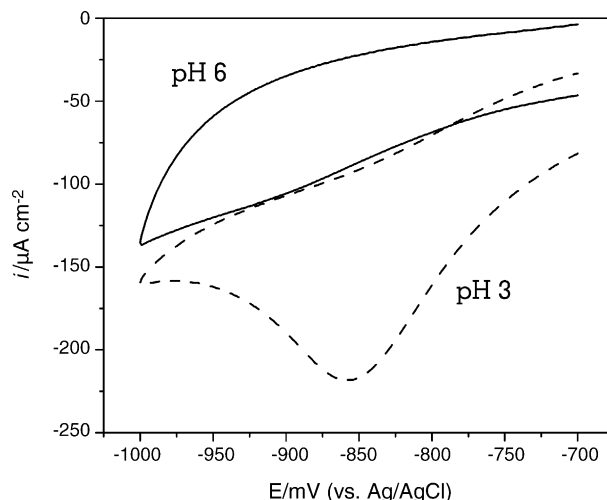


Fig. 3. Cyclic voltammograms of electrodeposited nickel in solutions containing 1 M Na_2SO_4 at pH 3 (dashed line) and pH 6 (full line). Scanning rate 20 mV s^{-1} .

centrations reaction (8) becomes the rate-controlling step [17].

Anodic branches of cyclic voltammograms contain a single anodic peak Ia, regardless of the solution pH. The low ratio of anodic to cathodic charge (insets in Fig. 2a and b) indicates incomplete nickel oxidation, which was also confirmed by Philip and Nicol, who suggested that formation of passive film in ammoniacal solutions leads to incomplete nickel oxidation [25]. To survey the electrode surface conditions after the completion of peak Ia, the cyclic voltammograms were cycled three times, in order to build sufficient amount of a reaction product. It was found that with repeated cycling the onset of cathodic peak became more positive by 200–400 mV, and that the magnitude of cathodic and anodic peaks increased.

AFM examination of the electrode was performed for two characteristic potentials: (1) at the crossover potential of the first cv cycle and (2) at the beginning of the second cv cycle (Fig. 4a–d).

Nickel clusters appear to be well defined at the crossover potential for each studied pH (Fig. 4a and c), but their appearance becomes “fuzzy” at the end of anodic branch (Fig. 4b and d). The fuzzy appearance of nickel clusters, including the visible horizontal streaks, is characteristic for the AFM tip–sample interaction with the soft, powdery phase, extricated by the AFM tip, resulting in reduced image quality. The exact nature of the nickel oxidation products (hydroxide, oxide) or the mechanism of nickel passivation was not determined, as this was beyond the scope of the present study.

3.3. Chronoamperometry and nucleation modeling

3.3.1. Effect of deposition potential

The mechanisms of nickel nucleation from ammoniacal solutions were examined by employing the chronoamperometric (ca) technique. The ca-s were initiated from 0 mV to a

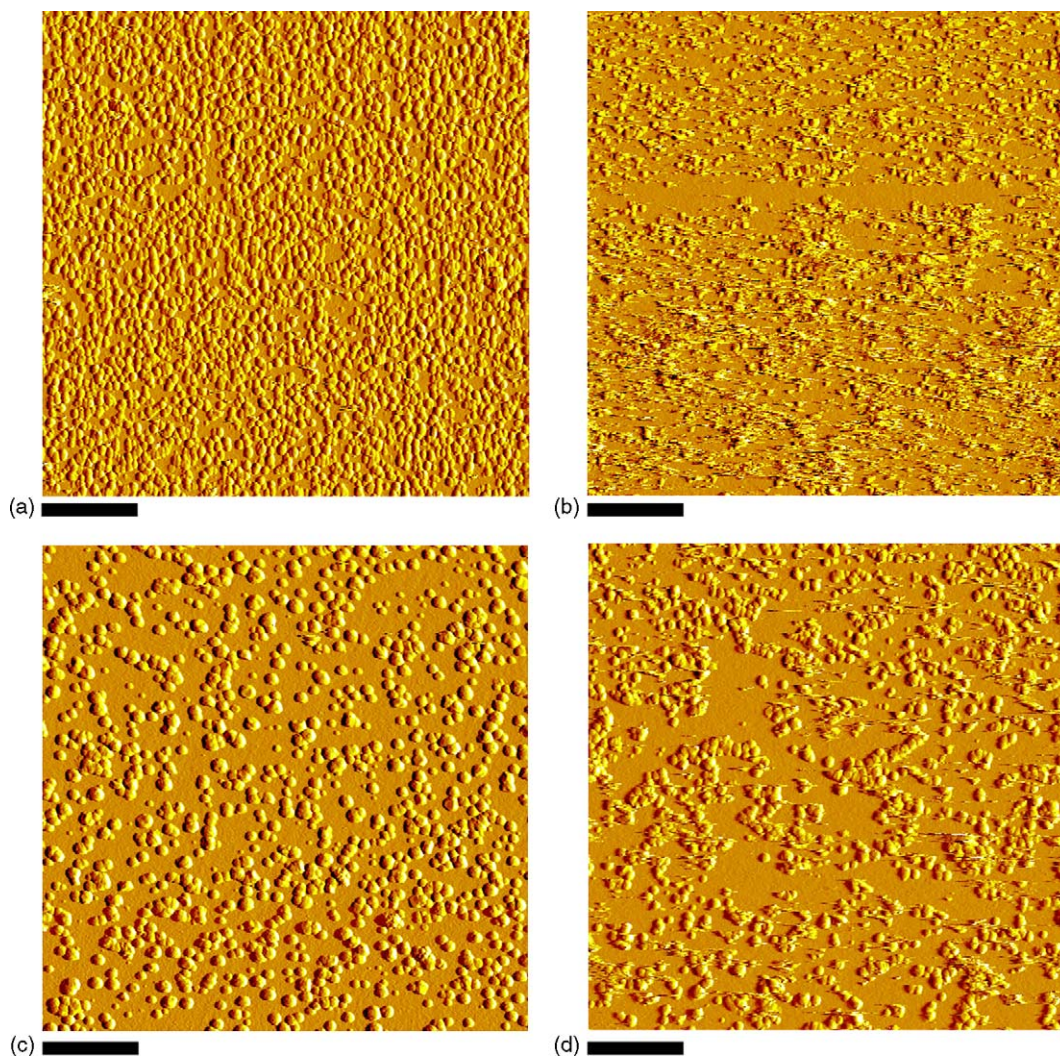


Fig. 4. AFM of the electrode surface at two characteristic cv potentials: pH 6—(a) crossover of the first cv (-960 mV); (b) onset of the second cv (0 mV); pH 9—(c) crossover of the first cv (-980 mV); (d) onset of the second cv (0 mV). Conditions: 0.01 M Ni^{2+} ; 1 M $(\text{NH}_4)_2\text{SO}_4$; scanning rate 20 mV s^{-1} , scale bar 1 μm .

range of deposition potentials, chosen from the cv-s in Fig. 2a and b to be more negative than the peak I_c . Recorded current transients are presented in Fig. 5a–d.

The mechanisms of nickel nucleation were compared to the theoretical models derived by Scharifker and Hills [26]. The models utilize the coordinates of the ca peaks in order to distinguish between the two limiting nucleation mechanisms: *instantaneous* and *progressive*. Instantaneous nucleation corresponds to immediate activation of all nucleation sites, and the rate of further nuclei formation is negligible in the time frame of the experiment. During progressive nucleation, the rate of new nuclei formation in the time frame of the experiment is not negligible. Instantaneous and progressive nucleation models are represented by Eqs. (10) and (11), respectively:

$$\frac{i^2}{i_m^2} = \frac{1.9542}{\frac{t}{t_m}} \left\{ 1 - \exp \left[-1.2564 \left(\frac{t}{t_m} \right) \right] \right\}^2 \quad (10)$$

$$\frac{i^2}{i_m^2} = \frac{1.2254}{\frac{t}{t_m}} \left\{ 1 - \exp \left[-2.3367 \left(\frac{t}{t_m} \right)^2 \right] \right\}^2 \quad (11)$$

where i_m and t_m are the current and the time, as respective peak coordinates. Data from Fig. 5a–d are replotted in Fig. 6a–d with reduced current-time coordinates, along with the theoretical models for instantaneous and progressive nucleation.

According to Fig. 6a–d, nickel nucleation follows the progressive nucleation model, regardless of the solution pH or nickel concentration. Negative deviation of chronoamperograms from the models at around $t/t_{\text{max}} = 2$, was also observed by others [11], although on gold substrate and from ammonia-free solutions. The observed negative deviation from the model is most likely related to reduction of hydrogen ions and hydrogen evolution. The simultaneous increase in levels of current plateaus with more cathodic deposition potentials under all experimental conditions in Fig. 5a–d is a clear indi-

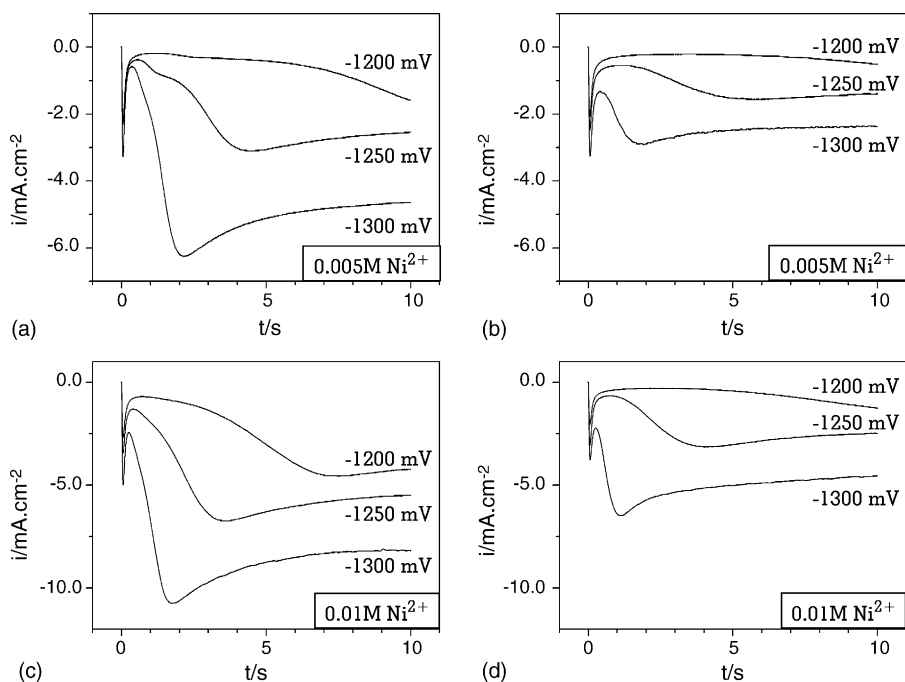


Fig. 5. Chronoamperometric deposition of Ni as a function of pH and Ni concentration in 1 M $(\text{NH}_4)_2\text{SO}_4$: (a and b) pH 6 and (c and d) pH 9.

cator of the additional current due to hydrogen ions reduction that causes the observed deviation from the models. This invalidates the interpretation of the results in Fig. 6, because the model given by Eqs. (10) and (11) cannot distinguish between the currents contributed by the nickel ion and hydrogen ion reduction.

Scharifker–Hills model also allows the type of nucleation to be determined by analyzing the ascending parts of the chronoamperograms, prior to the overlap of nuclei diffusion zones. At this stage, the reduction of hydrogen ions is not so prominent, and majority of current corresponds to reduction of nickel ions. The ascending portions of the current–time

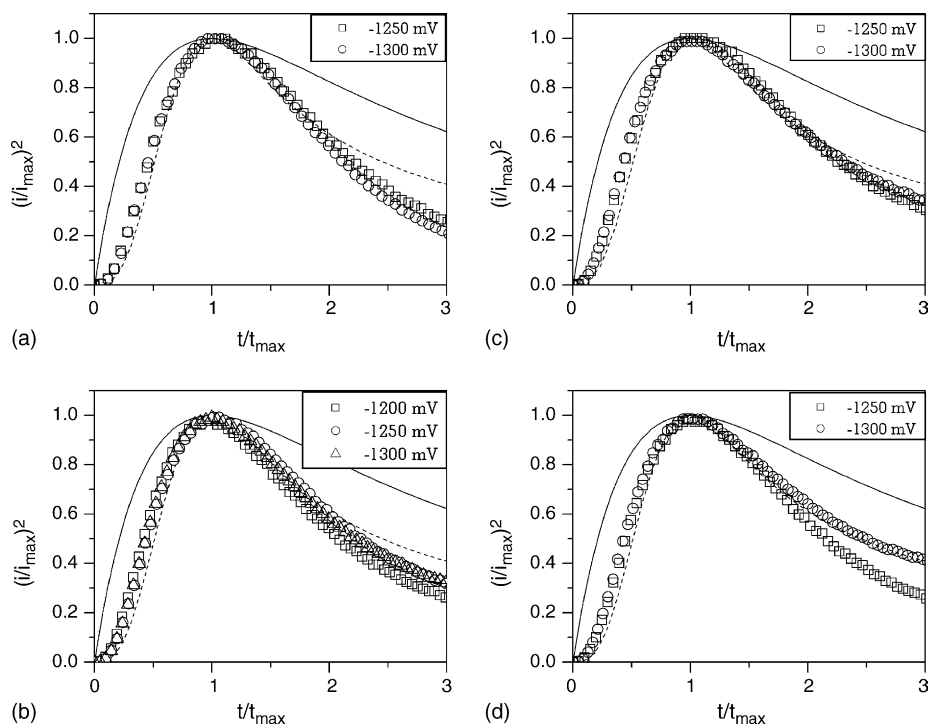


Fig. 6. (a–d) Chronoamperograms from Fig. 5a–d presented in reduced current–reduced time coordinates. Theoretical models for instantaneous and progressive nucleation are represented by solid and dashed lines, respectively.

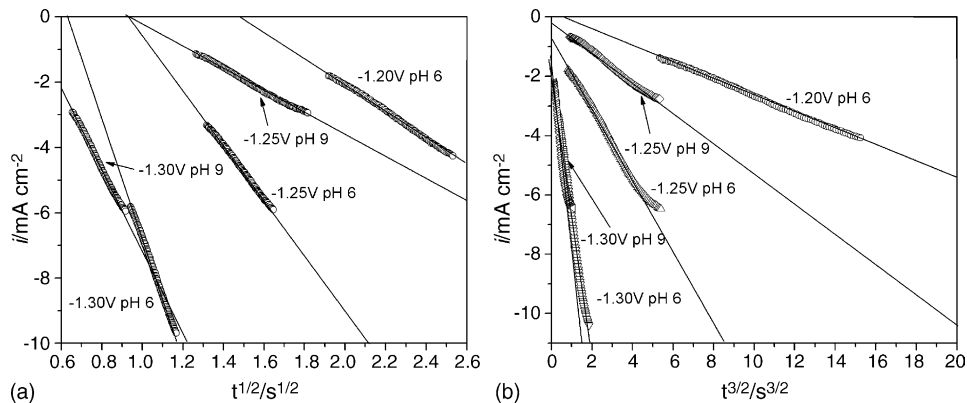


Fig. 7. Ascending parts of the current time transients (symbols) in: (a) $i-t^{1/2}$ and (b) $i-t^{3/2}$ domain. Nickel concentration 0.01 M.

transients should exhibit linear dependence in either the $i-t^{1/2}$ or $i-t^{3/2}$ domains, for instantaneous and progressive nucleation mechanisms, respectively [26] (Fig. 7a and b).

The results in Fig. 7a and b indicate that the initial portions of chronoamperograms can better be linearized in the $i-t^{1/2}$ domain, which corresponds to the instantaneous nucleation regime. It should be noted that the linearization is not ideal in either of the two domains.

Because of the apparent discrepancy in the assigned nickel nucleation mechanisms, which change depending on the employed diagnostic criteria, a newly proposed nucleation model by Palomar-Pardave et al. which takes into account the contribution from the concurrent hydrogen ion reduction, was also used [27]. The model, given by Eq. (12) represents the sum of the metal ion and hydrogen ion current contributions:

$$i_{\text{total}}(t) = (P_1^* + P_4 t^{-1/2}) \times \left(1 - \exp \left\{ -P_2 \left[t - \frac{1 - \exp(-P_3 t)}{P_3} \right] \right\} \right) \quad (12)$$

Complete definition of the parameters P_1^* , P_2 , P_3 and P_4 is given in Appendix A. The two parameters most relevant for

the type of nucleation mechanisms are P_2 and P_3 :

$$P_2 = N_0 \pi k D \quad (13)$$

$$P_3 = A \quad (14)$$

where N_0 is the density of nucleation sites, A the rate of nucleation, $k = (8\pi c_0/\rho)^{0.5}$, c_0 the concentration of metal ion, ρ the deposit density and D is the diffusion coefficient of metal ions. The comparison between the two experimental chronoamperograms and the current–time transients that were generated by the non-linear Marquardt–Levenberg fitting algorithm is presented in Fig. 8a and b.

Parameters P_1^* , P_2 , P_3 and P_4 were varied during the curve fitting, and are presented in Table 1 for some of the chronoamperograms from Fig. 5a–d.

According to Table 1, both A and the N_0 increase with more cathodic deposition potentials. The rate of new nickel nuclei formation per active site is slow, with only 10^{-5} to 10^{-4} new sites activated per second, compared to the 10^{-1} s^{-1} to 10^{-2} s^{-1} when cobalt is deposited [27]. The density of nucleation sites on the other hand is on the order of 10^{10} cm^{-2} to 10^{11} cm^{-2} , which is higher than that of cobalt deposited on the same substrate, where the theoretical density of the nucleation sites was on the order of 10^6 cm^{-2} [27], while

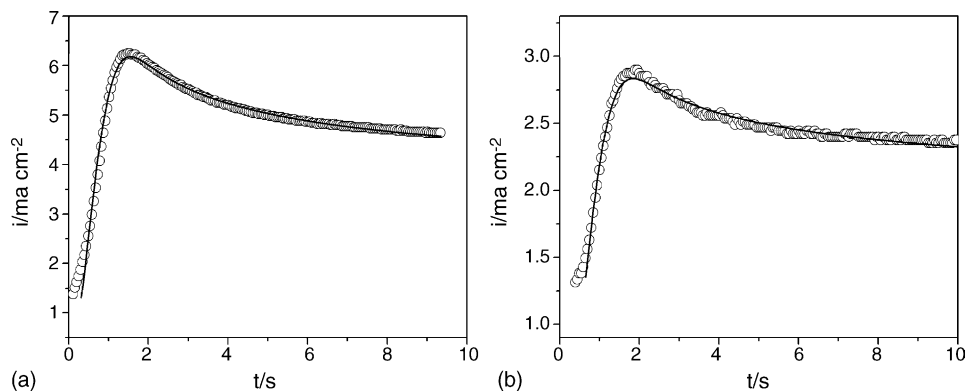


Fig. 8. Comparison between the experimental chronoamperograms (symbols) at: (a) pH 6 and (b) pH 9 and the theoretical current transients (solid lines) obtained by fitting the expression (12) to the experimental data. Conditions: 0.005 M Ni^{2+} ; $E_{\text{dep}} = -1300 \text{ mV}$.

Table 1
Values of the parameters P_1^* , P_2 , P_3 and P_4 , obtained by non-linear fitting of the experimental chronoamperograms from Fig. 5a–d with Eq. (12) [27]

$[\text{Ni}^{2+}]$ (M)	E_{dep} (mV)	P_1^* (mA cm^{-2})	P_2 (s^{-1})	P_3 (s^{-1})	P_4 ($\text{mA cm}^{-2} \text{s}^{0.5}$)	A (s^{-1})	N_0 (cm^{-2})
0.005							
pH 6	–1250	1.03	11858	3×10^{-5}	4.34	3×10^{-5}	1.00×10^{11}
	–1300	3.31	28907	1×10^{-4}	3.85	1×10^{-4}	2.45×10^{11}
pH 9	–1250	0.04	7519	2×10^{-5}	3.22	2×10^{-5}	6.37×10^{10}
	–1300	1.89	28826	8×10^{-5}	1.36	8×10^{-5}	2.44×10^{11}
0.01							
pH 6	–1250	3.27	9823	6×10^{-5}	6.53	6×10^{-5}	5.88×10^{10}
	–1300	5.64	18975	9×10^{-5}	7.22	9×10^{-5}	1.14×10^{11}
pH 9	–1250	0.92	9193	4×10^{-5}	4.67	4×10^{-5}	5.50×10^{10}
	–1300	3.57	29630	1.7×10^{-4}	3.18	1.7×10^{-4}	1.77×10^{11}

the experimentally determined cluster population densities were on the order of 10^9 cm^{-2} to 10^{10} cm^{-2} [28]. It follows that the initial nickel nucleation on a very large number of active nucleation sites exhausts their further availability, thus limiting the growth of nickel deposit to the already formed nuclei. This scenario corresponds to the instantaneous nucleation regime, and is in agreement with the results in Fig. 7a and b.

The effect of deposition potential on morphology of nickel clusters is presented in Fig. 9a–f.

According to Fig. 9a–f, the clusters population density at pH 6 is much higher than at pH 9. This may likely be the result of higher surface coverage by adsorbed nickel–sulfate complex at pH 6, than by nickel–amino complex at pH 9, as discussed above.

At pH 6 (Fig. 9a–c), there is an increase in the clusters population density between –1200 mV and –1250 mV, with uniform surface coverage. However, the last image in this series shows coarsening of nickel clusters, with regions of barren glassy carbon still visible. The evidence for coarsening of the clusters was previously found in the studies of nickel electrodeposition on pyrolytic graphite [13] and in the studies of cobalt electrodeposition on glassy carbon [28]. Both studies suggest that hydrogen evolution is responsible for the aggregation of small clusters into larger ones during the course of electrodeposition, presumably by physical interaction between hydrogen bubbles and nickel clusters. Another considered explanation, the aggregation of nickel clusters due to magnetostatic interactions, was unlikely because the average diameters of nickel clusters found in this study were below the calculated superparamagnetic–ferromagnetic limit of the face centered cubic nickel spherical particles (78 nm) [29].

At pH 9, deposition at more cathodic potentials resulted in the increase of nickel clusters population density (Fig. 9d–f), without the coarsening effect observed at pH 6.

In order to better visualize the morphology of Ni-clusters in the earlier stages of development, the AFM examination was performed after two seconds of deposition, right after the formation of a chronoamperometric peak, i.e. at the time when diffusional zones overlapped. The AFM images, for solutions at pH 6 and pH 9, are presented in Fig. 10a and b.

According to Fig. 10a and b, nickel clusters are of uneven sizes in the early stages of deposition, a known characteristic for progressive nucleation mechanisms. The clusters size is very small, particularly at pH 6 where the average height of a nucleus is only several nanometers. Despite their small size, the overlapping clusters can be still visualized. At pH 9, the numerous overlapped (fused) clusters can readily be seen.

The morphology of nickel clusters electrodeposited from solutions with higher Ni concentration (0.01 M) is presented in Fig. 11a and b.

According to analysis of Fig. 11a, at pH 6, the increase of nickel concentration from 0.005 M to 0.01 M resulted in more than a three-fold increase of clusters population density N , from $1.5 \times 10^{10} \text{ cm}^{-2}$ to $5.5 \times 10^{10} \text{ cm}^{-2}$, respectively. At pH 9, Ni-clusters size increased for 0.01 M Ni^{2+} , but the clusters population density stayed constant to around $6 \times 10^9 \text{ cm}^{-2}$, irrespective of nickel concentration. The cluster population densities are well in agreement with the densities of active sites determined from the parameters of Eq. (12).

Qualitative interpretation of the degree of nucleation inhibition can be obtained from the $\log N$ versus η^{-2} plots, as the saturation clusters population density is proportional to nucleation overvoltage, η^{-2} [30]. Nucleation overvoltage, η , was determined as the difference between the deposition potential and the crossover between the cathodic and anodic current traces (the redox Ni^{2+}/Ni potential [20]). The values of redox potentials were –940 mV and –970 mV at pH 6 and pH 9, respectively.

According to the results in Fig. 12, the $\log N$ versus η^{-2} lines are characterized with very small slopes for all investigated conditions, an indication of the highly inhibited nucleation mechanisms. A high degree of inhibition is also consistent with the results obtained in the study of nickel deposition from ammonia-free solutions [10–15], and with the low rates on nucleation determined from Eq. (12).

3.3.2. Effect of solution temperature

The effect of solution temperature was investigated in the range 5–55 °C. Nickel electrodeposition was carried out at

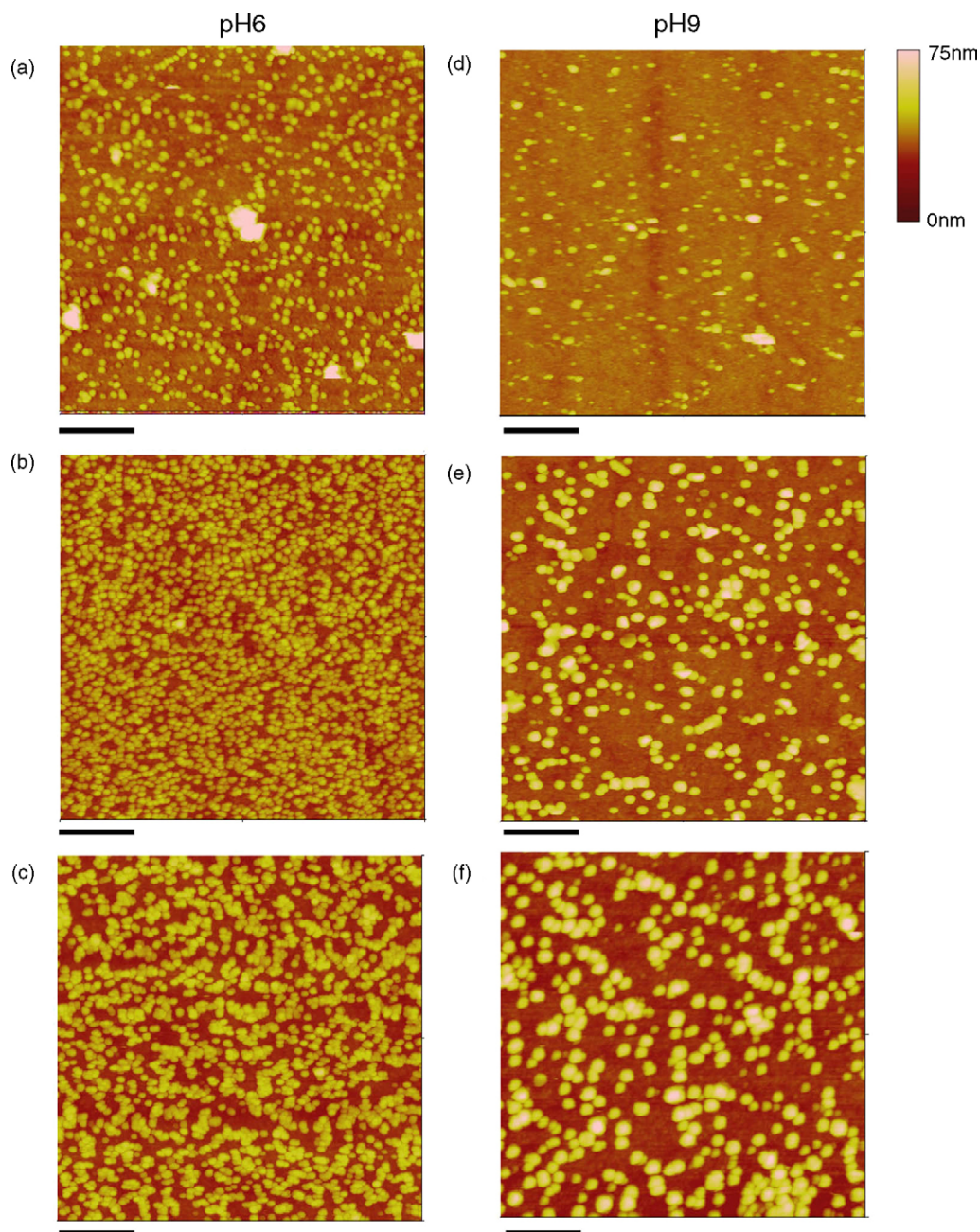


Fig. 9. AFM height images—effect of deposition potential on the morphology of electrodeposited nickel: pH 6—(a) -1200 mV, (b) -1250 mV and (c) -1300 mV; pH 9—(d) -1200 mV, (e) -1250 mV and (f) -1300 mV. Conditions: 0.005 M Ni^{2+} ; 1 M $(\text{NH}_4)_2\text{SO}_4$; scale bar 400 nm; vertical height scale range 0 – 75 nm.

-1250 mV for 10 s. from both pH 6 and pH 9 solutions. Reduced current transients (not presented here) indicate that nickel electrodeposition mechanisms remain progressive, regardless of the solution temperature for both pH 6 and pH 9. Clusters population densities as a function of temperature are presented in Fig. 13.

According to Fig. 13, the clusters population density follows the Arrhenius type of temperature dependence, Eq. (15):

$$N = A \times e^{-E_a/RT} \quad (15)$$

where N is the number of clusters, A the constant, E_a the activation energy, R the gas constant and T is the temperature. Increase in the clusters population densities with the increasing temperature is most likely related to the thermal activation of the glassy carbon electrode, and the consequent increase in the number of available active nucleation sites, and increasing mobility of nickel ions at elevated temperatures.

Different activation energies at pH 6 and pH 9, 15 kJ and 23 kJ, respectively, could be related to different desolvation pathways for ammino and aquo solvated nickel ions,

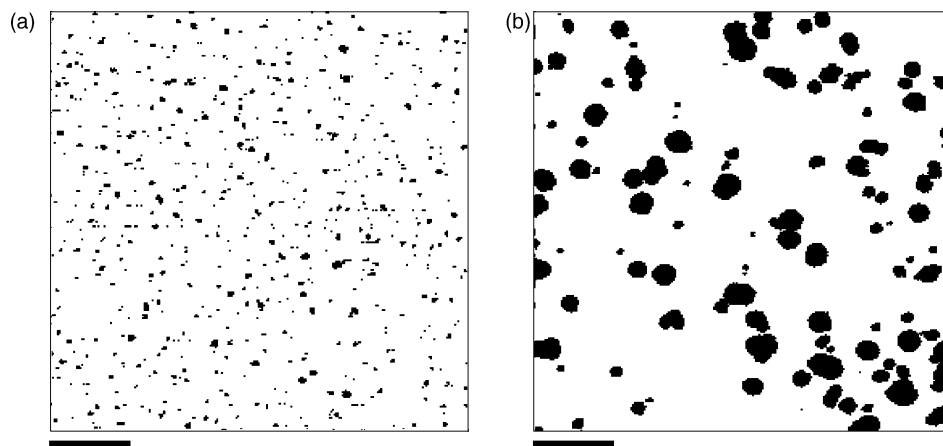


Fig. 10. Nickel clusters formed after 2 s of electrodeposition from: (a) pH 6 and (b) pH 9 solutions. Conditions: electrodeposition performed from 0.005 M Ni^{2+} + 1 M $(\text{NH}_4)_2\text{SO}_4$ solution at -1250 mV. Note that for clarity, the images are binary coded, black representing nickel clusters and white representing glassy carbon surface. Scale bar 200 nm.

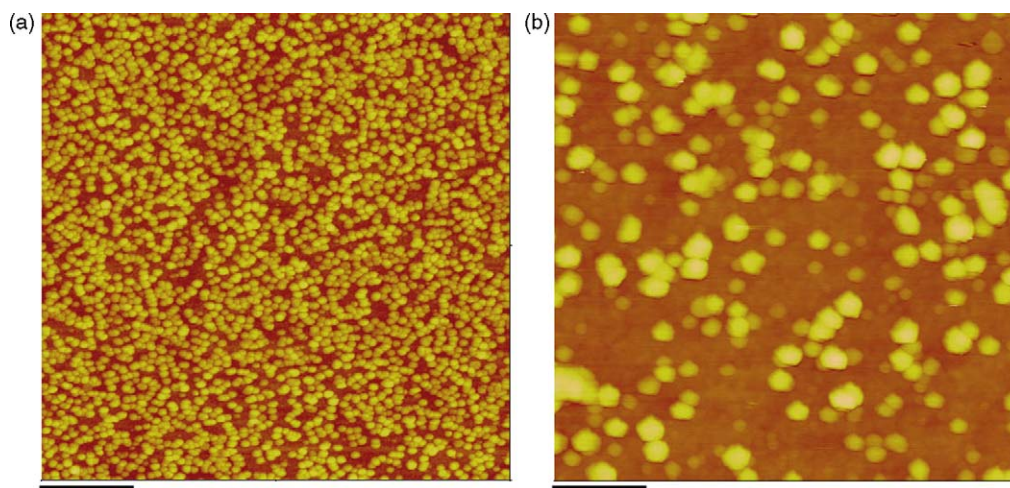


Fig. 11. AFM height images of nickel clusters deposited from 0.01 M Ni^{2+} + 1 M $(\text{NH}_4)_2\text{SO}_4$ solutions at: (a) pH 6 and (b) pH 9. Conditions: deposition potential -1200 mV; $t_{\text{dep}} = 10$ s; height = 75 nm; scale bar 400 nm (compare with morphology in Fig. 7a and d for deposition of Ni from 0.005 M Ni^{2+}).

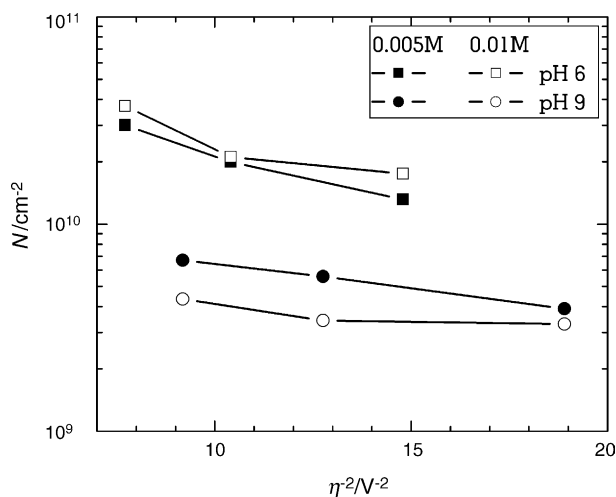


Fig. 12. Measured clusters population density as a function of deposition overvoltage.

similar to those calculated for cobalt [31]. Ab initio study by Mendoza-Huizar et al. [31] shows that desolvation of cobalt–amino complex is less energetically demanding process than the desolvation of cobalt–aquo complex, which was experimentally confirmed by the lower electrocrystallization overpotential of cobalt–amino complex [28,32]. In the present study, the electrocrystallization overpotential of nickel–amino complex is higher than that of nickel–aquo complex (Fig. 2a and b). Higher overpotential, together with higher activation energy found from the slope in Fig. 13 may indicate that the desolvation of nickel–amino complex represents energetically more demanding process. This conclusion could further be supported by an ab initio study of nickel–aquo–amino complex desolvation and electroreduction, similar to that for cobalt [31].

3.3.3. Effect of conditioning potential

The glassy carbon electrode was subjected to electrochemical conditioning at either +1 V or -1 V for 2 min in the

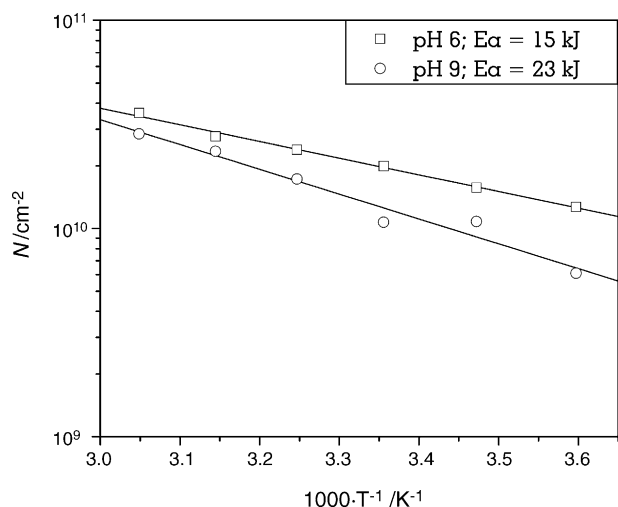


Fig. 13. Ni-clusters population density, determined from the AFM image analysis, as a function of temperature. Full lines are linear fits for data at pH 6 and pH 9. Conditions: $E_{\text{dep}} = -1250$ mV; deposition time 10 s; 0.005 M Ni^{2+} ; 1 M $(\text{NH}_4)_2\text{SO}_4$.

nickel-free solutions containing 1 M $(\text{NH}_4)_2\text{SO}_4$ at pH 6 or pH 9. Nickel was then deposited on the conditioned electrode chronoamperometrically for 10 s, at -1250 mV, from pH matching solutions containing 0.005 M Ni^{2+} . The morphology of electrodeposited nickel was then examined by the AFM. The electrode surface images, after the conditioning-deposition sequence, are presented in Fig. 14a–d.

According to Fig. 14a and c, conditioning at negative potentials results in reduction of clusters population density in both pH solutions. Electrode conditioning at positive potentials, on the other hand, results in a significant increase of clusters population density (Fig. 12b and d). Similar conditioning effect was observed earlier for copper electrodeposited from ammoniacal solutions [33]. The explanation for the observed effect is difficult to provide, because of the complex nature of glassy carbon surface with respect to the presence of oxide groups serving as catalysts for the electron transfer [34], and the unknown content of surface impurities.

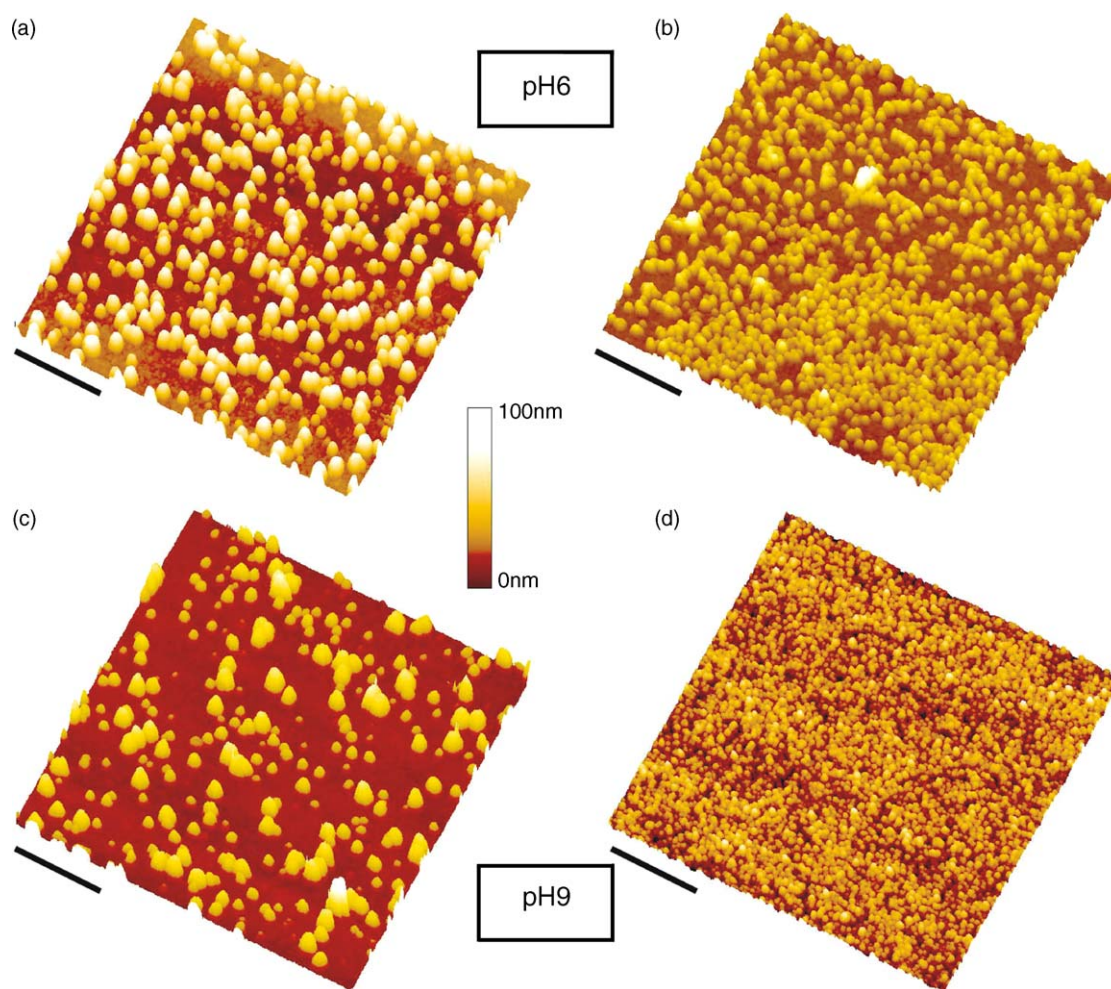


Fig. 14. The effect of electrochemical modification of the glassy carbon electrode on the size and population density of electrodeposited nickel clusters: pH 6—(a) $E_{\text{cond}} = -1$ V and (b) $E_{\text{cond}} = +1$ V; pH 9—(c) $E_{\text{cond}} = -1$ V and (d) $E_{\text{cond}} = +1$ V. Conditions: $E_{\text{dep}} = -1250$ mV; scale bar 500 nm.

4. Conclusions

The mechanisms of electrochemical deposition of nickel from ammoniacal solutions, on glassy carbon, were investigated by cyclic voltammetry and chronoamperometry. Corresponding nickel morphology was examined by atomic force microscopy. The following conclusions can be made:

1. Deposition involves two electrochemical and one chemical (adsorption) steps, i.e. nickel nucleates according to the ECE mechanisms. At pH 6, and low nickel concentration (0.005 M), adsorption of $\text{Ni}(\text{SO}_4)^-$ is fast. The rate of $\text{Ni}(\text{SO}_4)^-$ adsorption decreases with the increasing nickel concentration. At pH 9, the mechanisms are similar except that the adsorbing species are $\text{Ni}(\text{NH}_3)_m^+$, i.e. deposition happens from Ni–ammine complexes.
2. Electrodeposition of nickel is inhibited by SO_4^{2-} and hydrogen adsorption. According to the cyclovoltammetric and morphological studies, the degree of inhibition is higher at pH 6 than at pH 9.
3. Chronoamperometric study indicates that nickel nucleation conforms to the instantaneous nucleation mechanism, under all investigated conditions. The statistical analysis of AFM images showed higher clusters population density when nickel was deposited from sulfate (pH 6) than from amino complexing solutions (pH 9). Cluster population densities were on the same order as the theoretically calculated number of active sites.
4. Nickel clusters population density increased with the increase of solution temperature, following the Arrhenius type of dependence. The difference in calculated activation energies may be related to different energetic requirements for nickel–ammine and nickel–aquo ions desolvation. An ab initio study may be required for further confirmation.

Acknowledgements

This work has been sponsored by the U.S. Department of Defense, Department of the Navy, Office of Naval Research, Grant Number N000140110829, and The National Science Foundation RII Award (EPS 0132626).

Appendix A

This section contains definitions of parameters P_1^* , P_2 , P_3 and P_4 in Eq. (12). For further explanation refer to [27].

$$P_1^* = P_1 \left(\frac{2c_0M}{\pi\rho} \right)^{1/2}$$

$$P_1 = z_{\text{PR}} F k_{\text{PR}}$$

$$P_2 = N_0 \pi k D$$

$$P_3 = A$$

$$P_4 = \frac{2FD^{1/2}c_0}{\pi^{1/2}}$$

c_0 is the bulk concentration of metal ions, M the molar mass of deposit, ρ the density of deposit, $z_{\text{PR}}F$ the molar charge transferred during the proton reduction process, k_{PR} the rate constant of the proton reduction reaction, N_0 the density of nucleation sites, $k = (8\pi c_0/\rho)^{0.5}$, D the diffusion coefficient of metal ions and A is the rate of nucleation.

References

- [1] W.H. Remington, U.S. Patent 82,877 (1868).
- [2] I. Adams, U.S. Patent 93,157 (1869).
- [3] O.P. Watts, *Trans. Am. Electrochem. Soc.* 23 (1916) 395.
- [4] M. Abyaneh, *Electrochim. Acta* 27 (1982) 1329.
- [5] M. Abyaneh, M. Fleischmann, *Electrochim. Acta* 27 (1982) 1513.
- [6] M. Abyaneh, W. Visser, E. Barendrecht, *Electrochim. Acta* 28 (1983) 285.
- [7] J. Amblard, M. Froment, G. Maurin, N. Spyrellis, E. Trevisan-Souteyrand, *Electrochim. Acta* 28 (1983) 909.
- [8] Chr. Bozhkov, Chr. Tzvetkova, St. Rashkov, *J. Electroanal. Chem.* 296 (1990) 453.
- [9] E. Gomez, C. Muller, R. Pollina, M. Sarret, E. Valles, *J. Electroanal. Chem.* 333 (1992) 47.
- [10] M. Fleischmann, A. Saraby-Reintjes, *Electrochim. Acta* 29 (1984) 69.
- [11] A.N. Correia, S.A.S. Machado, L.A. Avaca, *J. Electroanal. Chem.* 488 (2000) 110.
- [12] A.G. Munoz, D.R. Salinas, J.B. Bessone, *Thin Solid Films* 429 (2003) 119.
- [13] E. Chassaing, M. Jousselein, R.J. Wiert, *J. Electroanal. Chem.* 157 (1983) 75.
- [14] R. Wiert, *Electrochim. Acta* 35 (1990) 35.
- [15] A. Saraby-Reintjes, M. Fleischmann, *Electrochim. Acta* 29 (1984) 557.
- [16] W. Davison, J.A. Harrison, *J. Electroanal. Chem.* 36 (1972) 399.
- [17] H.I. Philip, M.J. Nicol, *The Electrodeposition of Nickel from Ammoniacal Solutions*, Project Report No. 1804, National Institute for Metallurgy, Randburg, South Africa, April 1976.
- [18] M.P. Zach, R.M. Penner, *Adv. Mater.* 12 (2000) 878.
- [19] H.-H. Huang, *STABCAL—Stability Calculation for Aqueous Systems*, Montana Tech of the University of Montana, Butte, MT.
- [20] Southampton Electrochemistry Group, in: T.J. Kemp (Ed.), *Instrumental Methods in Electrochemistry*, Ellis Horwood Ltd., Chichester, UK, 1985.
- [21] A. Lachenwitzer, O.M. Magnussen, *J. Phys. Chem. B* 104 (2000) 7424.
- [22] P. Broekmann, M. Wilms, K. Wandelt, *Surf. Rev. Lett.* 6 (5) (1999) 907.
- [23] M. Wilms, P. Broekmann, C. Stuhlmann, K. Wandelt, *Surf. Sci.* 416 (1998) 121.
- [24] J.W. Yan, J.M. Wu, Q. Wu, Z.X. Xie, B.W. Mao, *Langmuir* 19 (2003) 7948.
- [25] M.J. Nicol, W.M. Stapleton, A.N.E. Balaes, *An Electrochemical Investigation of the Dissolution of Copper, Nickel and Copper–Nickel Alloys in Ammonium Carbonate Solutions*, Project Report No. 1630, National Institute for Metallurgy, Randburg, South Africa, May 1974.
- [26] B. Scharifker, G. Hills, *Electrochim. Acta* 28 (7) (1983) 879.
- [27] M. Palomar-Pardave, B.R. Scharifker, E.M. Arce, M. Romero-Romo, *Electrochim. Acta* 50 (2005) 4736.
- [28] D. Grujicic, B. Pesic, *Electrochim. Acta* 49 (2004) 4719.

- [29] B.D. Cullity, Introduction to Magnetic Materials, Pearson Addison Wesley, Boston, MA, 1972, p. 614.
- [30] A. Serruya, J. Mostany, B.R. Scharifker, J. Electroanal. Chem. 446 (1999) 39.
- [31] L.H. Mendoza-Huizar, M. Palomar-Pardave, J. Robles, Electrochim. Acta 46 (2001) 2749.
- [32] M. Palomar-Pardave, I. Gonzales, A.B. Soto, E.M. Arce, J. Electroanal. Chem. 443 (1998) 125.
- [33] D. Grujicic, B. Pesic, Electrochim. Acta 50 (2005) 4426.
- [34] P. Chen, R.L. McCreery, Anal. Chem. 68 (1996) 3958.